JGR Solid Earth

Author Contributions:
Conceptualization: Annemarieke Béguin, Karl Fabian
Data curation: Annemarieke Béguin
Formal analysis: Annemarieke Béguin
Investigation: Annemarieke Béguin
Methodology: Annemarieke Béguin
Resources: Suzanne A. McEnroe
Software: Annemarieke Béguin
Validation: Annemarieke Béguin
Visualization: Annemarieke Béguin, Nathan S. Church
Writing – original draft: Annemarieke Béguin, Karl Fabian

Quantifying Internal Stress and Demagnetization Effects for Natural Multidomain Magnetite and Magnetite-Ilmenite Intergrowths

Annemarieke Béguin[1], **Karl Fabian[1]**, **Nathan S. Church[1]**, and **Suzanne A. McEnroe[1]**

[1]Norwegian University of Science and Technology (NTNU), Trondheim, Norway

Abstract Demagnetizing effects and internal stress are difficult to distinguish in natural magnetite samples, but quantitative stress estimates can provide valuable information about microstructure formation, surface oxidation, impacts, tectonic stresses, or interface properties in exsolution structures. Quantifying demagnetizing effects informs about magnetite particle shape, magnetostatic interaction, or anisotropic texture. Here, we establish an improved measurement workflow to separate demagnetizing effects from internal stress for natural magnetite. The method is based on temperature-dependent hysteresis measurements, and for natural samples require accurate estimates of Curie temperature and temperature-dependent saturation magnetization to ensure that near-end-member magnetite is the dominant magnetic mineral, and to calibrate the temperature-dependent scaled reversible work (SRW). SRW is the fundamental quantity to determine stress and demagnetizing factor. The improved SRW method is applied to three natural samples with different stress histories where it proves that large magnetite crystals in the metamorphosed Modum complex (Norway) have low internal stress (<100 MPa), while in highly exsolved magnetite-ilmenite intergrowths from Taberg (Sweden) and Bushveld (South Africa) the magnetite component is highly stressed (>230 MPa). This confirms experimentally that interface strain in complex microstructures due to spinodal decomposition and partial oxidation creates large average internal stress in the magnetite minerals. Because sister specimens have similar internal stress but noticeably (>20%) different demagnetizing factors, textural, and shape anisotropy contribute substantially to SRW in these samples.

Plain Language Summary Magnetite is one of the most abundant magnetic minerals in nature and an important magnetic recorder over the entire history of the Earth. In natural rocks even chemically pure magnetite particles vary considerably in size, shape, and internal stress. Hitherto, mainly the variation in size has been systematically studied, partly because there was no experimental way to reliably quantify stress and shape effects. We now use a new technique to quantify stress and shape effects in three natural magnetite mineral types. One which formed millions of years ago at elevated temperature shows very little shape and stress influences. In the other two samples, slowly cooled magnetite formed a very fine network of lamellae at nanometer scale. In these cases, it was theoretically predicted that internal stress should reach values of up to 300–600 MPa at the interface. For the first time, we can experimentally verify that the high average stresses of up to 340 MPa indeed occur in these exsolution structures. The successful test of our new method extends the toolbox of rock magnetism by a valuable additional technique to quantify previously unknown internal properties of natural magnetite.

1. Introduction

Magnetite grains within terrestrial and planetary rocks retain information on the past states of ambient fields, but also react magnetically to internal stress, particle shape, and particle distribution. Both the ability to acquire a magnetic remanence and the resulting magnetic stability are controlled by the magnetization states of these grains, which depend on particle size, geometry, magnetostatic particle interaction, and the state of internal stress (Dunlop, 2021). Although magnetite is the best-studied natural magnetic mineral, many processes of how these properties affect remanence acquisition, and possibly enhanced remanence intensity, remain enigmatic (McEnroe et al., 2022).

The importance of internal stress in magnetite has been discussed for over 50 years (Hodych, 1973, 1977, 1982, 1986, 1996; Hodych & Matzka, 2004; Lindquist et al., 2015; Moskowitz, 1993; Shive & Butler, 1969; Stacey & Wise, 1967; ter Maat et al., 2020; Yuan et al., 2019), but an experimental quantification proved difficult. The

Writing – review & editing:
Annemarieke Béguin, Karl Fabian,
Nathan S. Church, Suzanne A. McEnroe

main challenge is that magnetite is a soft magnetic material (Hubert & Schäfer, 1998), such that a quantitative investigation requires the separation of small stress energies from large demagnetizing energies.

Béguin and Fabian (2021) showed that this separation can be achieved by analyzing the scaled reversible work (SRW) at different temperatures. This SRW method is closely related to the first studies of the approach-to-saturation (ATS) region in hysteresis curves, which established micromagnetism as a separate research field (Akulov, 1930, 1931; Kersten, 1932). In rock magnetism, reversible magnetization work at room temperature (RT) has been studied before (Appel, 1987; Appel & Soffel, 1984; Fabian, 2003), but for magnetite its application as a stress indicator was hampered by the large demagnetizing field (Hodych, 1990).

So far, the SRW method has been developed and validated for synthetic magnetite samples (Béguin & Fabian, 2021). In natural samples, the SRW method faces additional difficulties related to high-temperature alteration, low signal-to-noise ratios (SNRs), and impurity or inhomogeneity of the natural magnetite minerals. We here develop an SRW workflow for natural magnetite and apply it to a selection of rock samples which covers the extreme ends of the expected stress distribution. One sample from Modum, Norway, is expected to contain stress-free end-member multidomain (MD) magnetite grains. Two other samples (Bushveld, South Africa; Taberg, Sweden) contain magnetite with abundant submicrometer exsolution. Both are expected to yield high magnetostatic interaction. Their lamellar interfaces have been theoretically predicted to potentially create substantial internal stress due to interface strain (Price, 1981), but it has never been experimentally tested the extent to which this strain is accommodated by plastic deformation via dislocation arrays (Robinson et al., 2016), or retains it in a state of coherent elastic stress.

2. The Concept of the SRW Method

Demagnetizing energies in magnetite particle ensembles change with temperature exactly proportional to

$$K_d(T) = \frac{1}{2}\,\mu_0\,M_s(T)^2$$

where μ_0 is the vacuum permeability, and $M_s(T)$ is the saturation magnetization as a function of temperature T, which varies between $M_{s,0} = 512{,}188$ A/m (Pauthenet & Bochirol, 1951) at $T = 0$ K and 0 A/m at the Curie temperature $T_C \approx 580°$C. Because stress and magnetocrystalline anisotropy energies have substantially different temperature dependencies, the SRW method uses a set of hysteresis curves at several temperatures between RT and T_C to separate these anisotropies from the demagnetizing energy (Béguin & Fabian, 2021). The key part is a careful analysis of the reversible magnetization change in the ATS region, where relatively small changes in magnetization occur at relatively large magnetic fields (Figure 1a). Magnetic fields B are scaled relative to saturation induction $J_s(T) = \mu_0 M_s(T)$ to obtain $b = B/J_s(T)$. Magnetizations M are scaled by $M_s(T)$, such that all scaled magnetization curves $m(b) = M(B)/M_s(T)$ approach the value of 1 in the limit of large b. For the scaled temperature $\tau = 1 - T/T_C$, the SRW $w_{rev}(\tau)$ is then defined as the area above the scaled curve, but below 1, in a temperature-independent scaled field interval $[b_1, b_2]$ (Figure 1b).

Natural samples behave less ideally in the SRW method of Béguin and Fabian (2021) due to alteration at elevated temperatures, and also because their Curie temperature is commonly less distinct than in synthetic magnetite (Jackson & Bowles, 2018). In rapidly cooled systems, exsolution from an initial titanomagnetite solid solution may be incomplete, resulting in a distribution of phases close to the magnetite end-member. We therefore here describe an improved SRW evaluation to robustly calculate $w_{rev}(\tau)$ for natural samples.

Most magnetometers measure magnetic moments $\mu = MV$ (A m^2), where V is the unknown volume of the magnetite fraction in the sample. To apply the SRW method, μ is therefore scaled by the magnetic saturation moment $\mu_s = M_s(T)\,V$, such that $m(b) = \mu(B)/\mu_s(T)$ and V needs to be known because scaling of B requires $M_s(T) = \mu_s(T)/V$. The estimation of μ_s and V proceeds in two steps. First, the high-field hysteresis curve $\mu(B)$ of the specimen is corrected for linear variation due to a combined diamagnetic and paramagnetic susceptibility χ, which also accounts for possible sample-holder diamagnetism. This is achieved by fitting $\mu(B)$ at each temperature to the ATS-law (Fabian, 2006)

$$\mu(B) \;=\; \mu_s + \chi\,B + \alpha\,B^\beta \tag{1}$$

This provides estimates for $\mu_s(T)$, $\chi(T)$, $\alpha(T)$, and $\beta(T)$.
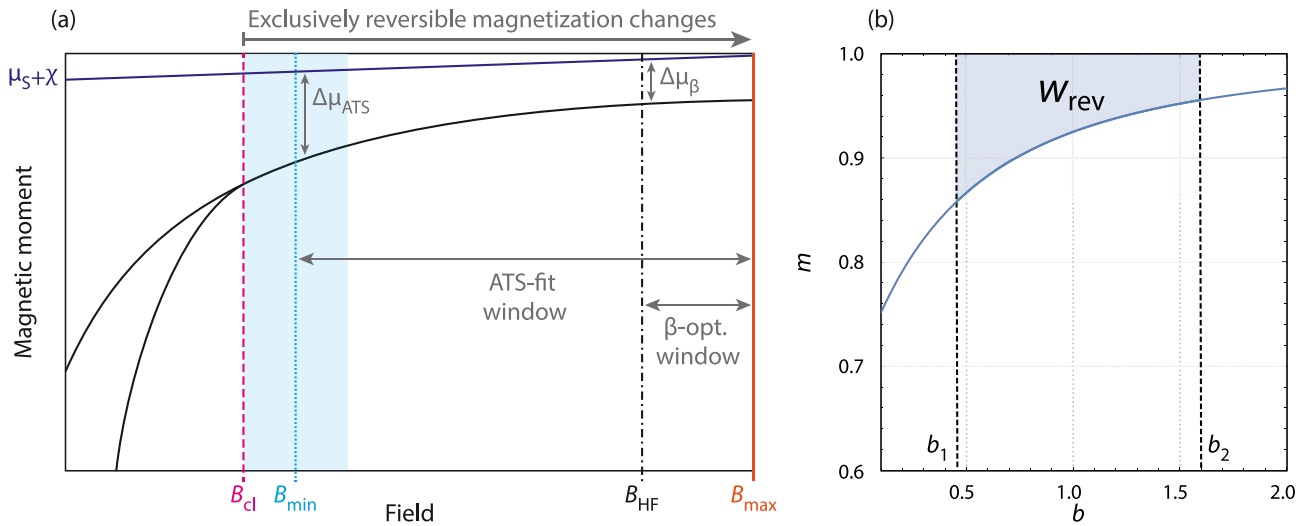
Figure 1. (a) In the approach-to-saturation (ATS) region above the closure field B_{cl}, only reversible magnetization changes occur. The ATS-fit window $[B_{min}, B_{max}]$, in which the parameters μ_s, χ, α, and β of Equation 1 are determined, is chosen as an optimal compromise between temperature variation, saturation, and measurement noise. The high-field region between B_{HF} and B_{max} defines the β-optimization window. (b) After scaling the moment by the saturation moment and B by J_s one obtains the unit free scaled plot of the upper hysteresis branch $m(b)$, from which the scaled reversible work w_{rev} is calculated by integrating $1 - m(b)$ over the scaled field interval $[b_1, b_2]$.

In the second step, the temperature-dependent $\mu_s(T)$ is fit to the theoretical power law

$$\mu_s(\tau) = M_{s,0}\, V\, \tau^\gamma, \quad \text{with} \quad \tau = 1 - \frac{T}{T_C} \tag{2}$$

Because $M_{s,0}$ for magnetite at 0 K is known (Pauthenet & Bochirol, 1951), this provides best-fit estimates for V, T_C, and the critical exponent γ.

For the fit of the ATS-law (Equation 1), it is essential to determine the optimal field interval window in which no irreversible processes occur, but still covers a sufficiently large variation of the magnetic moment to ensure that all parameters of the ATS-law can be reliably determined with the best SNR. The condition that no irreversible processes occur can be met by choosing the minimal field B_{min} of the ATS-fit window larger than the closure field B_{cl} above which the upper and lower hysteresis branches coincide and only reversible magnetization changes occur. A theoretical upper limit for the closure field from single domain theory (McElhinny & McFadden, 1999; Néel, 1949; Stoner & Wohlfarth, 1948) is derived in Supporting Information S1, with a reasonable coercivity limit for magnetite particles as a scaled closure field of $b_{cl} \approx \Delta N \leq 0.45$. The relative position of the involved field values is sketched in Figure 1a.

3. Materials and Experimental Methods

3.1. Natural Magnetite-Bearing Samples From Three Case Studies

We use a suite of natural rock samples from three locations. For a metamorphosed serpentinite sample from the Modum complex, Southern Norway (Jøsang, 1966), which formed during the Sveconorwegian event (Munz & Morvik, 1991), thermomagnetic results by Pastore et al. (2019) confirm that end-member magnetite is the primary magnetic carrier. Pastore et al. (2019) report the mineral assemblage of the Modum sample to consists of serpentine, magnesite, and mm-cm-scale magnetite crystals with rare Mg-Al-spinel needles, and barite. The Modum specimens are therefore expected to represent low-stress MD magnetite. Higher internal stress is expected in our sample BS31 from a large mafic layered intrusion, the Bushveld Complex (South Africa). BS31 is from a magnetite gabbronorite from the Main Zone located south of Stoffberg in the Eastern lobe of the intrusion (Cawthorn et al., 2016). The third sample Ta comes from Smålands Taberg Ore deposit which is composed of olivine, titanomagnetite, and minor Ca-rich plagioclase. The titanomagnetite is exsolved into magnetite, spinel, and ulvöspinel (Hjelmqvist, 1950; Sandecki, 2000), which later oxidized to ilmenite. The cloth-textured ulvöspinel and magnetite in Ta were previously studied by Price (1979, 1980), who also

calculated a theoretical ulvöspinel-magnetite interface stress of 300–660 MPa (Price, 1981) that so far has not been confirmed experimentally.

3.2. Rock Magnetic Properties of Bulk Samples

To characterize the remanence-carrying iron oxides in the samples, bulk and microscopic measurements were performed at the NTNU rock magnetic laboratory.

The 2D geometry and oxidation state of the remanence-carrying iron oxides were assessed using scanning electron microscope (SEM) images obtained with a Phenom XL Desktop SEM. Images were taken at different magnifications to identify the presence and estimate the abundance and size of microstructures within the iron oxides (Figure 2). Our Modum sample is the same thin section as studied by Pastore et al. (2019). It contains an area of magnetite of ~1 cm × 4 cm surrounded by serpentinite and magnesite. The magnetite grains are homogeneous with rare small spinel exsolution needles. Both the Bushveld and the Taberg samples display cloth-textured intergrowths of ulvöspinel and magnetite. The exsolution wavelength for BS31 is ~500 nm and the grains have similar microstructures throughout. Ta shows longer exsolution wavelengths of ~1 μm with more complex patterns and areas subdivided by Al-pleonaste, typical for spinodal decomposition of titanomagnetite to magnetite plus ulvöspinel. Later the ulvöspinel oxidized to ilmenite, but retained the original (100) exsolution pattern.

Temperature-dependent bulk magnetic susceptibility $\chi_0(T)$ was measured using an AGICO MFK1A Kappabridge system with a CS-L Cryostat attachment for cooling to $T_{min} \approx 78$ K in liquid nitrogen, and a CS4 furnace attachment for heating in argon to $T_{max} = 650$°C. $\chi_0(T)$ was measured on heating between T_{min} and T_{max} and on cooling to RT. Lastly, $\chi_0(T)$ was measured again between T_{min} and RT after heating by repeating the low-temperature run. The results are shown in Figure 2 and Table S1 in Supporting Information S1. For the Modum sample, a Verwey transition temperature (T_V) of 107 K was observed from the steepest ascent from the low-temperature heating curves. Both the curves before and after heating to 900 K show similar results up until 200 K; however, the peak in susceptibility is ~2% higher for the preheating curve. The bulk susceptibility calculated from the high-temperature heating curve is 3% lower than the measured cooling curve, and a Curie temperature of 565°C was estimated from the Hopkinson peak temperature. For the Bushveld sample, the Verwey transition is less distinct, two samples were measured with T_V between 80 and 87 K. Susceptibility measured on heating results in a broad peak and T_C was estimated at 568°C from the linear fit of inverse susceptibility (Petrovský & Kapička, 2006). The cooling curve shows nonreversible behavior with largest offsets up to 16% at 800 K. The subsequent low-temperature measurement after heating does not yield a clear Verwey transition. This could indicate that this sample is thermally less stable than the Modum sample and possibly indicates some diffusion of Ti into the magnetite during heating. For the Taberg sample, a sharp Verwey transition was observed at $T_V = 91$ K, with similar heating and cooling curves showing small deviations of up to 3%. The T_C was estimated at 559°C from the sharp Hopkinson peak.

To experimentally verify the theoretical upper limit for the closure field (Supporting Information S1), the micro-coercivity distributions for our samples were measured by first-order reversal curves (FORCs) and nonlinear Preisach maps. These distributions were determined for each sample using a Princeton Measurements Corporation MicroMag 3900 Vibrating Sample Magnetometer (VSM) and the FORC distributions were calculated using FORCinel 3.06 (Harrison & Feinberg, 2008) (Figures 2g–2i). The maximum coercive field, field step, and number of curves were individually estimated from an RT full hysteresis curve. These acquisition parameters and the VARIFORC smoothing factors (Egli, 2013) are reported in Table S2 of Supporting Information S1. In agreement with its MD nature, the FORC diagram for the Modum sample has high densities of hysterons close to the B_u axis outside the region of stable remanent magnetizations. This indicates a prevalence of transient irreversible processes driven by the self-demagnetizing field (Fabian & von Dobeneck, 1997). The majority of the microcoercivities B_c visible in the FORC diagram appear to be below 10 mT both in the remanent and in the transient region of the diagram. FORC diagrams for the Bushveld and Taberg sample show essentially unimodal, slightly asymmetric hysteron densities with broad maxima close to $B_u = 0$, whereby the maximum for the Bushveld sample lies around $B_c = 18$ mT, and for Taberg around $B_c = 10$ mT. The Bushveld sample also displays a wider spread in B_u of >50 mT, whereas for the Taberg sample the corresponding spread is only about 30 mT. Nonlinear Preisach maps (Church et al., 2016) were used to obtain a clear upper limit of the maximal extent of the remanent coercivity distribution. From the diagrams in Figures 2j–2l, it is visible that all remanent hysterons have coercivities well below 200 mT. This experimentally limits all scaled closure fields to $b_{cl} < 0.41$. For the
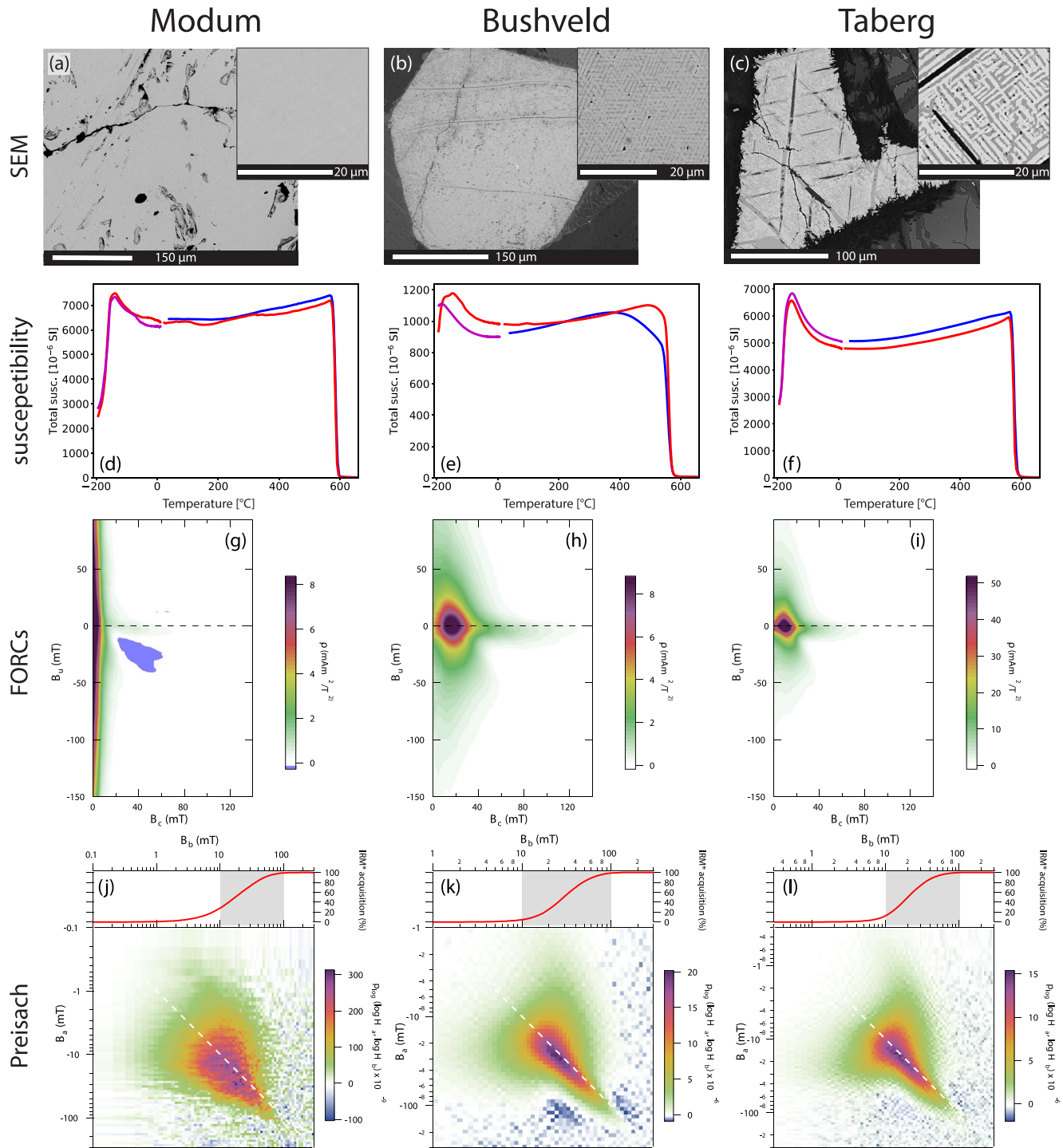
Figure 2. Scanning electron microscope (SEM) images (a and b) of the magnetite grains from Modum (Norway), Bushveld (South Africa), and Taberg (Sweden). The Modum sample displays a homogeneous magnetite multidomain mineral. For the two other samples, the SEM images show maze-like exsolution patterns of magnetite and ulvöspinel (now oxidized to ilmenite) with typical exsolution wavelengths of ∼500 nm (Bushveld) and 1 μm (Taberg). For the Taberg sample, the magnetite (beige) forms large scale connected regions with extremely large surface and complex interaction fields parallel to pleonaste (dark bands). Magnetic susceptibility $\chi_0(T)$ as function of temperature (c and d). The sample was first cooled to 90 K, $\chi_0(T)$ was measured during heating to room temperature (RT), and further to 650°C (red curve) and cooled back to RT (blue curve). Then the sample was cooled down to 90 K to measure a second $\chi_0(T)$ run on heating to RT (magenta curve). FORC diagrams of the rock specimens (g–i). In all cases, transient irreversible contributions occur at lower coercivities than remanent coercivities. Nonlinear Preisach maps (j–l) for three specimens clearly delineate the region of remanent irreversible coercivities and show that these vanish above a closure field of about 200 mT.

Modum sample, the remanent magnetic moments of the sample were very low and the data were smoothed using a 7×7 average filter before calculating of the Preisach diagram; the equivalent calculation using the original data is plotted in Figure S1 of Supporting Information S1.

3.3. Experimental Procedures

Because data quality is essential for a successful implementation of the SRW method, the measurement strategy focuses on acquiring high-quality, high-density data in the ATS region. For each of the three samples, two specimen chips with masses between 10 and 61 mg were prepared and measured on the VSM. The settings for the hysteresis measurements were chosen as those recommended in Béguin and Fabian (2021): the discrete measurement mode was used with a settling time of 250 ms and an averaging time of 600 ms. The initial curves and hysteresis curves were measured up to 1.08 T with 10 mT field increments. Specimens were first measured at RT, then were stepwise heated and measured in a He gas flow with temperature increments of 25°C up to 500°C. After each heating step, the specimen was allowed to thermally equilibrate for 300 s before the hysteresis branches were measured. To determine an independent Curie temperature with higher resolution, the above hysteresis measurements were directly followed by measuring M_{si}-curves (Fabian et al., 2013), with temperature increments of 2°C up to 600–650°C for one specimen of each sample (MOD-3, BS31-9, and Ta-3; Table S1 in Supporting Information S1).

High-field data on a Taberg sister specimen were measured using the Quantum Design Magnetic Property Measurement System (MPMS) at the Institute of Rock Magnetism, Minneapolis, USA. For Taberg specimen Ta-Ie-1, ATS curves were measured between RT and 500°C in 10 temperature steps, using the MPMS in discrete measurement mode with an averaging time of 5 s, and a maximum applied field of 2 T.

4. The Extended SRW Method for Natural Samples

Compared to synthetic magnetite (Béguin & Fabian, 2021), data from natural magnetite samples pose a number of new challenges to obtain robust SRW estimates. To reliably interpret the acquired temperature-dependent hysteresis data, we perform the following sequence of evaluation steps, an overview of the workflow is presented in Supporting Information S1.

4.1. High-Field Slope Correction—ATS-Fit Preferable Over Linear Fit

At each temperature, the SRW method needs to estimate the high-field paramagnetic and diamagnetic slope as precisely as possible. To achieve this, we fit the ATS-law (Equation 1) to the measured data to obtain estimates for χ and μ_s. The standard VSM procedure calculates a linear slope correction in the interval $[0.7\,B_{max}, B_{max}]$ by a linear fit that assumes $\alpha = 0$ in Equation 1. This procedure can be noticeably overestimate the paramagnetic and diamagnetic slope χ, and correspondingly underestimate the saturation moment μ_s.

This inaccuracy is visualized in Figures 3a–3c for four different linear-fit slope corrections of MPMS data from Ta-Ie-1, measured up to a maximum field of 2 T. The fits of χ and μ_s were obtained for four different cutoff field values, where B_{cutoff} was smaller than the maximally applied field of 2 T. The modeled values of $B_{cutoff} = 0.85$, 1.0, 1.5, or 1.95 T represent maximal field values for different instruments or measurement procedures. The saturation moment as function of temperature is lowest for the lowest B_{cutoff}. Correspondingly, the high-field slopes $\chi(T)$ are higher for lower B_{cutoff}. The obtained saturation moments in Figure 3b change with B_{cutoff}, with the largest offset at low temperatures. Only above 675 K, the saturation moment curves coincide. The $\mu_s(T)$ and $\chi(T)$ curves are closest for the higher B_{cutoff} fields, although there is still a difference between the two cutoff fields which might indicate that the sample did not saturate at this field.

The same data set and B_{cutoff} fields are tested for the ATS-law fit (Figures 3d and 3e). The 4 $\mu_s(T)$ and $\chi(T)$ curves overlap and the obtained saturation moments are indistinguishable. This indicates that $\mu_s(T)$ and $\chi(T)$ curves can be reliably obtained already with ATS-fits for $B_{cutoff} = 0.85$ T. In the next steps, we will therefore use the ATS-law to correct for the high-field slope and to determine $\mu_s(T)$.

4.2. Optimally Fitting the ATS-Law

The ATS-law (Equation 1) has a nonlinear dependence on μ_s, χ, α, and β, and these parameters are highly correlated and influence different regions of the fit. A robust determination is therefore complicated (Fabian, 2006;
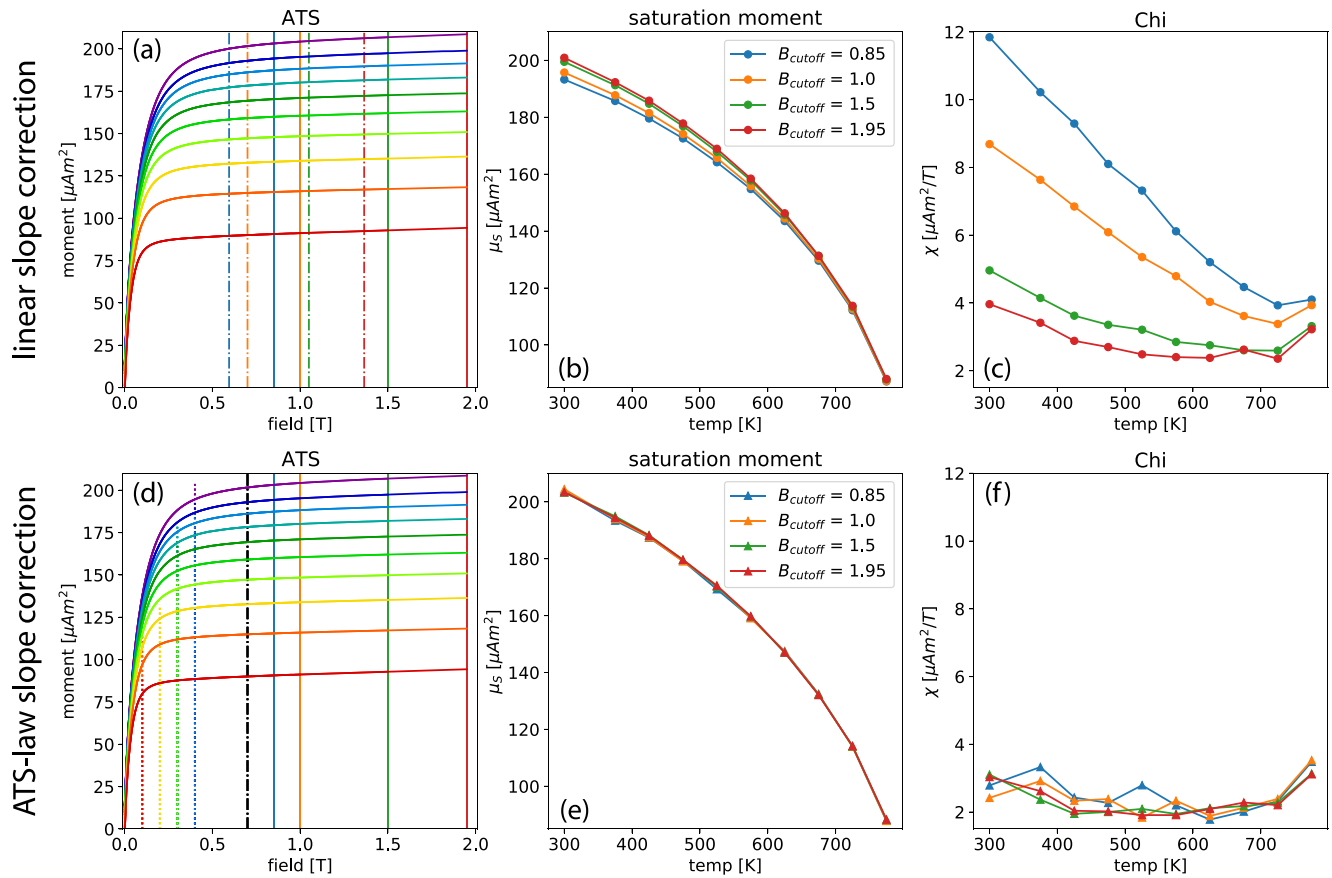
Figure 3. (a) Linear slope correction of magnetic moment versus field approach-to-saturation (ATS) data for specimen `Ta-Ie-1` measured up to 2 T, with increasing temperature starting from room temperature (RT, 300 K, purple curve), next 375 K (dark blue curve) and then in steps of 50° up to 775 K (red curve). The maximum cutoff fields are marked by solid vertical lines, B_{cutoff} = 0.85 T (blue), 1.0 T (orange), 1.5 T (green), and 1.95 T (red). The linear slope correction is calculated in the interval [0.7 B_{cutoff}, B_{cutoff}]. The lower end of this interval is indicated by dot-dash lines in the respective B_{cutoff} colors. The saturation moments (b) and high-field slopes (c) obtained for these B_{cutoff} values are plotted in the corresponding colors. An ATS-fit (d) to find the saturation moment and the high-field slope is used on the same high-temperature moment versus field data for specimen `Ta-Ie-1`, with the same B_{cutoff} values and the colors are as in (a). The high-field region is constant for all four options, with B_{HF} = 0.7 T (black dot-dash line). The region used for the ATS-fit is between a minimum field value, B_{min}, and the B_{cutoff} value. Where B_{min} decreased with increasing temperature, the dotted lines represent the B_{min} value used for each temperature step. Both the saturation moment (e) and high-field slope (f) behave similarly for all four B_{cutoff} values.

Jackson & Solheid, 2010). Which subset of the data is fit to the ATS-law influences the outcome of the fit and hence the value of the SRW. Here, we use a three-step procedure to find a suitable fit window for the ATS-law, i.e., the ATS-law fit window [B_{min}, B_{max}], using a high-field β-optimization window (Figure 1a). (a) For fixed values of B_{min} and β, the parameters μ_s, χ, α are determined by a best-fit procedure in the ATS-fit window. This is repeated for a range of β values between -3 and -1 using 0.01 increments. (b) For fixed B_{min}, the optimal value of β is the step 1 result with best-fit in the β-optimization window. (c) B_{min} is chosen to provide an overall smooth temperature dependence and optimal SNR from the step 2 results.

The ATS-law fit window is the field interval [B_{min}, B_{max}] in Figure 1a, where B_{min} is always chosen above the closure field B_{cl} of the hysteresis loop to guarantee that only reversible magnetization changes are fit. In case of $B_{min} = B_{cl}$, reversible magnetization change in the lower field regions of [B_{min}, B_{max}] may occur partially by complex reversible structural magnetization changes which we here broadly denote as "magnetization stretching" processes in contrast to the simple rotation of a homogeneous magnetization in the direction of the applied field. Magnetization stretching can saturate within the ATS-fit window and results in a net response that is poorly represented by the ATS-law (Equation 1) for low fields. If B_{min} is chosen too high; however, the ATS-fit window covers a too small moment range, or too few data points, which then leads to incorrect fitting of measurement noise. Accordingly, the maximum value of B_{min} should be chosen well below the value for which the nonlinearity F-test of Jackson and Solheid (2010) fails. To determine a suitable B_{min} value used for the ATS-fit, we compare

the resulting ATS parameters using multiple $B_{min}(T)$ curves based on the $B_{cl}(T)$ for the specimen. Here, we use up to five options for $B_{min}(T)$, namely $B_{cl}(T) < B_{opt.\ 1}, \ldots, B_{opt.\ 4}$, the values are listed in Table S3 of Supporting Information S1. These options are chosen to cover a range of fields from the closure field of the hysteresis loop, to twice this value. The main goal for using different $B_{min}(T)$ curve options is to identify from which field value the ATS data can be interpreted without interpreting the magnetization stretching effects. Beyond the magnetization stretching saturation field, the different options of B_{min} will give overlapping results within the measurement uncertainty.

For each $B_{min}(T)$ option, the ATS-fit window $[B_{min}, B_{max}]$ can be determined at each temperature. In this window, the measured moments $\mu(B)$ at each temperature are fitted to the ATS-law (Equation 1) for a range of β values between -3 and -1 using 0.01 increments. From the range of β values, we select as the optimal value that with the lowest L_2-norm misfit to the data contained in the β-optimization window (Figure 1a) between $0.7\ T < B < B_{max}$.

Measurement noise influences the minimum misfit that can be obtained by fitting the data. We therefore calculate a local noise level and determine the signal-to-noise in our ATS-fit window and β-optimization window. To calculate the local noise level in the region $[B_{min}, B_{max}]$, we use a robust fit to the measurement data and calculate the two-standard deviation. This is done by moving a small window of p points along the $[B_{min}, B_{max}]$ window and calculating the standard deviation of the robust fit to data. A quadratic spline fit though $p = 12$ points gives the initial fit. Then the three points with the highest deviation from the spline are removed and a second quadratic spline fit through the remaining nine points yields a robust fit to the data. The standard deviation of the region $[B_{min}, B_{max}]$ is the mean of the standard deviations for all local windows. The double standard deviation corresponds approximately to the 95% confidence interval δ_{95}. This robust local noise level is used to determine the SNR for the β-optimization and the ATS-fit windows. Because the reversible work is the area between the ATS curve and the saturation moment the signal magnitudes in the two windows are approximately $\Delta\mu_\beta$ and $\Delta\mu_{ATS}$, respectively (Figure 1a). The corresponding SNRs are thus

$$\text{SNR}_\beta = \frac{\Delta\mu_\beta}{\delta_{95}}, \quad \text{and} \quad \text{SNR}_{ATS} = \frac{\Delta\mu_{ATS}}{\delta_{95}}$$

A primary constraint for optimizing the measurement quality and for the choice of the fit windows, i.e., the selection of $B_{min}(T)$, is to obtain SNRs $\gg 1$. Furthermore, the misfit in the ATS-fit window and the β-optimization window was also divided by the two-standard deviation local noise. For a misfit in the respective window to be in the same order, or smaller than the local noise, the proxy should preferably be below 1. Moreover, the temperature-dependent ATS parameters for the options of $B_{min}(T)$ give insight into the robustness of the data interpretation. For a too low $B_{min}(T)$, the curves of $\mu_s(T)$, $\beta(T)$, $\alpha(T)$, $\chi(T)$, and hence $w_{rev}(\tau)$, will be offset due to the magnetization stretching processes. For a too high $B_{min}(T)$ curve, however, the curves of the ATS parameters are constrained by fewer data points, and could be influenced by fitting of measurement noise, thereby resulting in less-smooth curves. The visual comparison of the temperature ATS-parameter results in therefore important.

For the MPMS measurements only the ATS region between 2 and 0 T is measured, therefore the closure field B_{cl} cannot be directly determined from the MPMS data and the routine to find the optimal ATS-fit window at each temperature step is modified. When $B_{cl}(T)$ is unknown, for each temperature step we use a range of B_{min} values between 0.5 and 0.1 T and find the most suitable B_{min} value. For each candidate B_{min} value, the ATS-fit routine is repeated and the optimal β value for that B_{min} value is again that which gives the lowest misfit within the β-optimization window. To choose the best B_{min} value, we look for the lowest B_{min} value for which the optimal β values converges to a stable value. This process is repeated for each temperature step and results in an optimized $B_{min}(T)$ curve for the MPMS data.

4.3. Scaling the Temperature-Dependent ATS Curves

By repeating the above steps for all temperatures, we obtain the saturation moment as function of temperature, $\mu_s(T)$. With this information, it is possible to scale the measured moment by the saturation moment at each temperature step. From the theoretical power law (Equation 2), the Curie temperature and magnetite volume are obtained, and hence the saturation moment can be converted to saturation magnetization M_s.

To find the best fitting average Curie temperature directly from the ATS data, we rewrite Equation 2 by first introducing a reference volume $V_0 = 10^{-11}\ m^3$, corresponding to a 1% volume fraction of magnetite for a sample volume of 1 mm^3
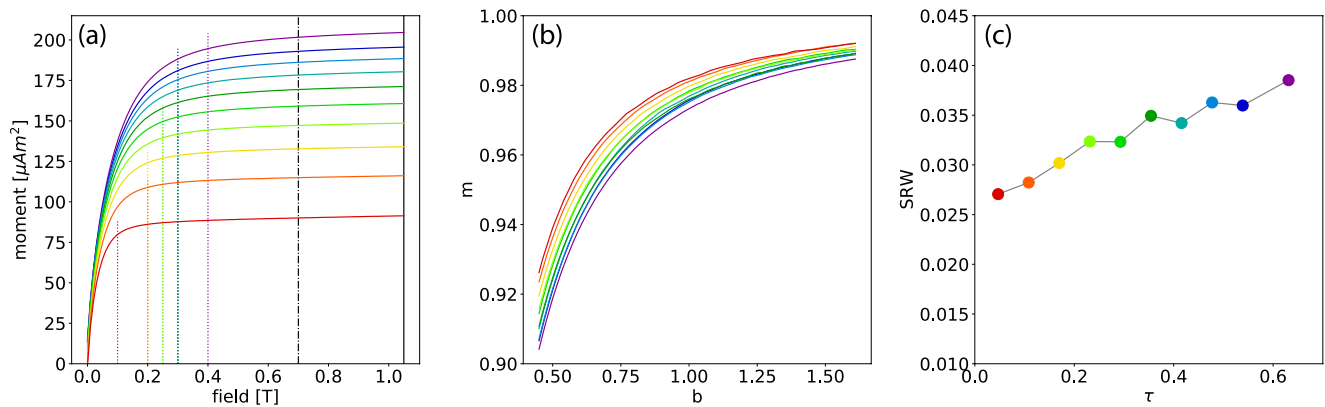
Figure 4. The magnetic moment versus field approach-to-saturation (ATS) data for specimen `Ta-Ie-3` measured on the Magnetic Property Measurement System (MPMS) (a) are given by the colored curves, the $B_{\min}$ values change with temperature (corresponding colored dotted lines). The maximum field value used for the ATS-fit was set to $B_{\max} = 1.05$ T (black line), and the high-field region for the β-optimization window was set to $B_{\mathrm{HF}} = 0.7$ T (black dashed line). From the scaled moment versus scaled field (b) curves, the SRW is determined and is plotted versus scaled temperature (c). The color code for temperature is the same as in Figure 3.

$$\mu_s(\tau) = \mu_{s0} \frac{V}{V_0} \left(1 - \frac{T}{T_C}\right)^{\gamma}, \quad \text{with} \quad \mu_{s0} = M_{s,0} V_0$$

Among a range of tentative Curie temperatures, we select the optimal T_C which yields the best straight-line fit of $\log(\mu_s(T)/\mu_{s0})$ versus $\log(1 - T/T_C)$. For this T_C, the intercept at $\log\left(1 - \frac{T}{T_C}\right) = 0$, where $T = 0$, gives $\mu_s(T = 0)/\mu_{s0} = V/V_0$, and thus an estimate for the specimen magnetite volume V. After dividing the saturation moment by V to obtain the saturation magnetization, it is finally possible to also scale the field values by J_s, such that the scaled moment can be plotted versus scaled field in Figure 4b.

The area above the curves of scaled moment versus scaled field in the fixed interval $[b_1, b_2]$ in Figure 4b defines $w_{\mathrm{rev}}(\tau)$, the SRW. Where b_1 should be chosen above the scaled closure field. The experimentally verified upper limit for the scaled closure field for our samples is $b_{\mathrm{cl}} < 0.41$. We can therefore use the same scaled field values $[b_1, b_2] = [0.45, 1.6]$ as in Béguin and Fabian (2021), and plot the temperature-dependent $w_{\mathrm{rev}}(\tau)$ in Figure 4c. By extrapolating this plot to $\tau = 0$, we obtain $w_{\mathrm{rev},0} = w_{\mathrm{rev}}(\tau = 0)$ and the linear slope $\partial_\tau w_{\mathrm{rev},0}$. These measured values can be compared to the numerical models for different ΔN and σ and thus provide quantitative estimates for both parameters. For the stress model of Béguin and Fabian (2021), λ_{111} is assumed to be the dominant magnetostriction constant for magnetite where mineral interfaces are involved (Klapel & Shive, 1974). If the temperature dependent polycrystalline magnetostriction constant λ_s (Moskowitz, 1993), would be used, the stress value could be overestimated since λ_{100} and λ_{111} have opposite signs. The region for the linear fit of the stress model in Béguin and Fabian (2021), was $0 < \tau < 0.45$. Here, we reinterpret the model curves with $0 < \tau < 0.3$, because the model values for larger τ values are nonlinear due to the temperature dependence of $\lambda_{111}(T)$. Revised approximations for the quantitative estimates are then given by

$$\Delta N \approx 2.82 \sqrt{w_{\mathrm{rev},0}}, \quad \text{and} \quad \sigma \approx 2.0\,\mathrm{GPa} \sqrt{\partial_\tau w_{\mathrm{rev},0}}$$

4.4. SRW at RT Versus Orientation Angle

As $w_{\mathrm{rev},0}$ reflects geometrical effects, the values may be different due to different shape or textural anisotropy of the specimens. Whether an individual specimen has a sufficiently high anisotropy can be tested by rotating it within the VSM, and measuring the SRW w_{rev} as function of orientation. At the NTNU VSM, there is not much space to rotate the sample when the furnace is inserted, and even a small wobble from the sample rod could possibly risk instrument damage. A set of rotation experiments was therefore performed after the high-temperature SRW experiments at RT without installed furnace. As a consequence of removing the furnace, the electromagnets have been moved. The pole gap was approximately the same in both experimental setups. The specimens were recemented to the ceramic holders. Initial curves and hysteresis loops were measured with 30° rotational increments

at RT after the high-temperature routine. For the ATS-fit, a constant value for $B_{\min}$ was used. To calculate the RT w_{rev} for all orientations, we used the corresponding T_C and V obtained from the high-temperature SRW sequence.

5. Results of the SRW Method for Natural Samples

5.1. ATS-Fit Window

For all specimens, the evaluation steps of the last section were systematically performed for different values of $B_{\min}$ as a function of temperature. The optimal choice depends on the individual nature of the reversible alignment processes for each specimen. For the VSM data, the closure field B_{cl} of the measured hysteresis loops was the first $B_{\min}(T)$ curve option. The relevant plots to determine $B_{\min}(T)$ for Ta-1 are collected in Figure 5; the results for the other specimens are available in Figures S2–S6 of Supporting Information S1. For Ta-1, the $B_{\min} = B_{\text{opt. 1}}$ and $B_{\min} = B_{\text{opt. 2}}$ lead to overlapping results for $\mu_s(T)$, $\beta(T)$, $\alpha(T)$, $\chi(T)$, and $w_{\text{rev}}(\tau)$ with deviations of <10% from one another. With $B_{\min} = B_{\text{cl}}$ higher $\mu_s(T)$ and $\beta(T)$ and lower $\alpha(T)$ and $\chi(T)$ curves were obtained, where the differences decrease with increasing temperature. This implies a higher $w_{\text{rev}}(\tau)$ curve. The $w_{\text{rev}}(\tau = 0)$ for $B_{\min} = B_{\text{cl}}$ is 0.022, and both $B_{\text{opt. 1}}$ and $B_{\text{opt. 2}}$ have $w_{\text{rev},0}$ values of 0.023. The temperature-dependent offset between the $w_{\text{rev}}(\tau)$ curve of $B_{\min} = B_{\text{cl}}$ and $B_{\min} = B_{\text{opt. 1}}$ indicate that the ATS-fit range used for $B_{\min} = B_{\text{cl}}$ is influenced by magnetization stretching processes. Both $B_{\text{opt. 1}}$ and $B_{\text{opt. 2}}$ are good candidates for the $B_{\min}$ curve and are both beyond the magnetization stretching saturation fields; we will use $B_{\text{opt. 1}}$ as this provides a smoother curve for $w_{\text{rev}}(\tau)$. The other Taberg specimen, Ta-3, behaves similarly and $B_{\min} = B_{\text{cl}}$ is also influenced by magnetization stretching processes. For this specimen, we will also use $B_{\text{opt. 1}}$. For the Bushveld specimens, the three $B_{\min}$ option curves give nearly indistinguishable results. From the signal-to-noise and misfit-to-local noise in the ATS-window, we identify a slight preference for $B_{\min} = B_{\text{opt. 1}}$ for specimen BS31-4 and $B_{\min} = B_{\text{cl}}$ for specimen BS31-9. For the Modum specimens, higher $B_{\min}$ option curves ($B_{\text{opt. 3}}$ and $B_{\text{opt. 4}}$) were used as both $B_{\text{opt. 1}}$ and $B_{\text{opt. 2}}$ have fields below the closure fields of these specimens. Although the results for the different $B_{\min}$ curves are comparable, the signal-to-noise and the misfit scaled to the local noise curves determined the best option. For MOD-1, the best option is $B_{\text{opt. 4}}$, and for MOD-2, the optimal $B_{\min}$ curve is $B_{\text{opt. 3}}$.

For the MPMS measurements of Ta-Ie-1, the $B_{\text{cl}}(T)$ curve was unknown. An optimized $B_{\min}(T)$ was obtained, using the convergences of β for a range of possible $B_{\min}$ values. For example, at a temperature of 300 K, for $B_{\min} = 0.3$ T $\beta = -1.67$, while for $B_{\min} = 0.4$ and 0.5 T $\beta = -1.7$. The lowest $B_{\min}$ value for which β converges at 300 K was chosen as $B_{\min} = 0.4$ (Figure 5, Table S3 in Supporting Information S1).

5.2. Magnetite Volume and T_C

With the optimal ATS-window per specimen, the Curie temperature, and the magnetite volume of the specimens were obtained (Table S1 and Figure S7 in Supporting Information S1). The highest Curie temperatures were obtained for the Modum specimens, 570 and 580°C; the Bushveld specimens have lowest Curie temperatures of 534 and 540°C; and the Taberg specimens have intermediate Curie temperatures of 560 and 566°C. The M_{si}-curve measurements (Figures S8–S10 in Supporting Information S1) result in similar T_C estimates for Modum (579°C) and Taberg (563°C). For the Bushveld specimen, the M_{si}-curve T_C estimate of 564°C differs from the power-law fit T_C estimate of 540°C for the same specimen.

The magnetite volumes are between $V = 3.85 \times 10^{-10} - 17.40 \times 10^{-10}$ m^3. These are proportional to the sample masses, and highest mass-normalized volumes are obtained for the Modum specimens with the largest magnetite contribution. Values of the power-law exponent γ are between $\gamma = 0.340 - 0.379$, up to 15% lower than the common literature value of 0.4 (Dunlop & Özdemir, 1997), but in agreement with other experimental values (e.g., Tauxe, 2010, Figure 3.8).

5.3. SRW Results

With the optimal $B_{\min}$ curves and Curie temperatures, the temperature-dependent moment versus field data was interpreted in terms of scaled moment as function of scaled field and the SRW was plotted versus scaled temperature (Figure 6 and Figure S11 in Supporting Information S1). For the Modum specimens, the scaled moment curves plot on top of one another, where for the Bushveld and Taberg specimens, the scaled moment
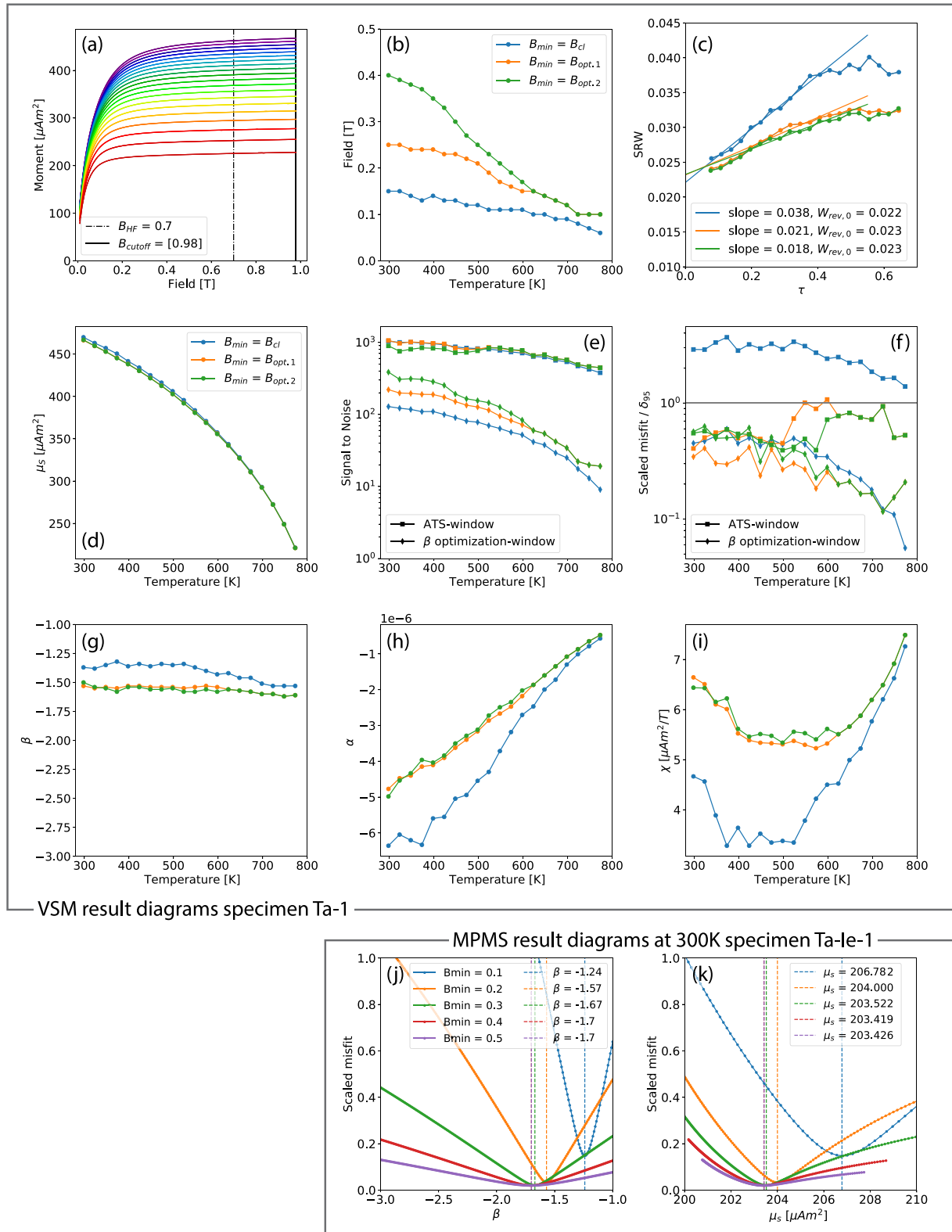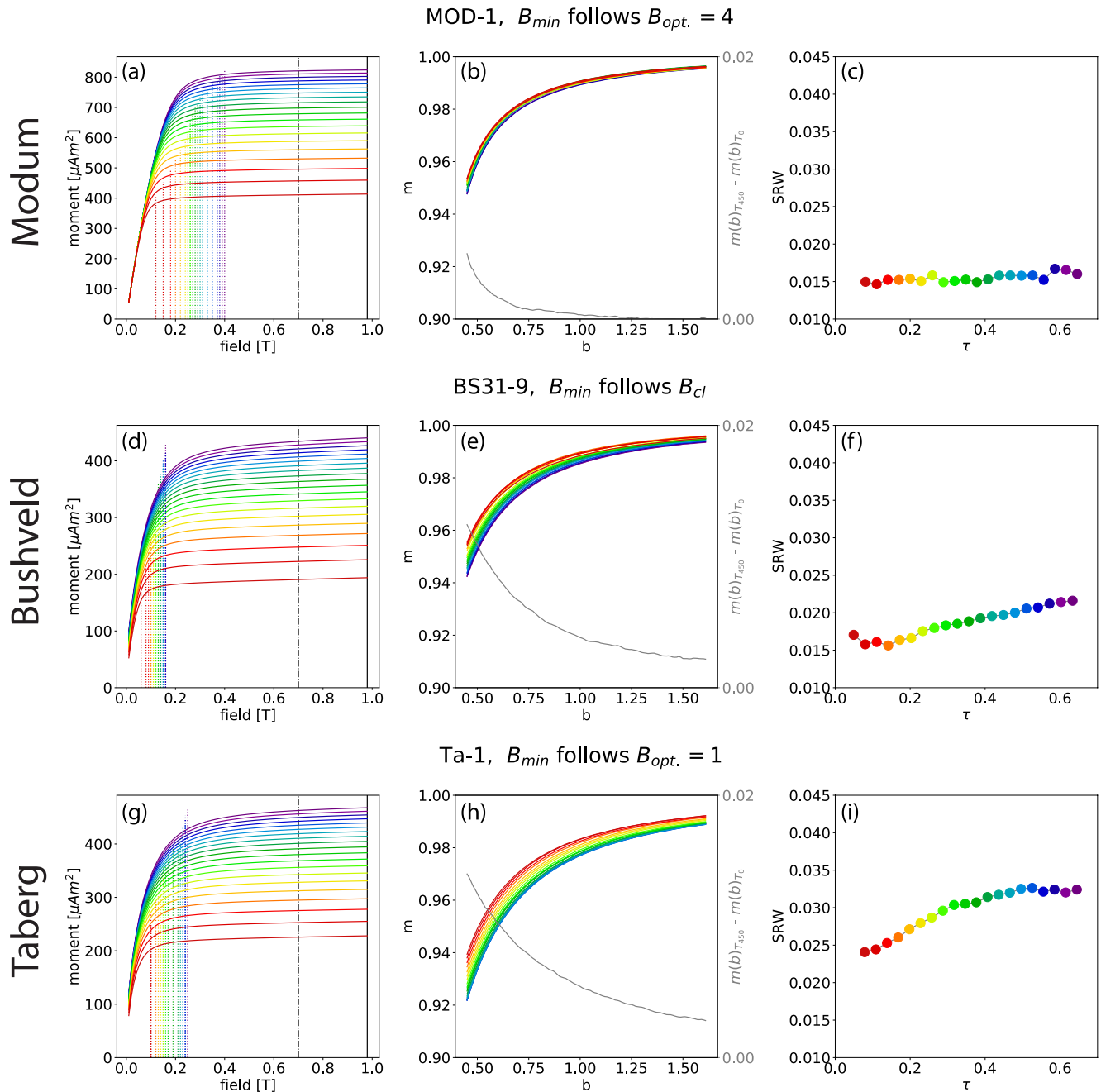
Figure 5.

Figure 6. Typical results for moment versus field, scaled moment versus scaled field, and scaled reversible work (SRW) versus scaled temperature τ for Modum Serpentinite (MOD-1, a–c), Bushveld (BS31-4, d–e), and Taberg (Ta-1, g–i) specimens. The color code for temperature is the same as in Figure 5a. The used B_{min} value is given in corresponding color (a, d, g), the $B_{max} = 0.98$ T (black line), and $B_{HF} = 0.7$ T (black dashed line). The gray line in the scaled moment versus scaled field plots (b, e, h) is the difference between the scaled moment versus scaled field curve at 450°C and RT.

Figure 5. Scaled reversible work (SRW) evaluation results for two Taberg specimen, Ta-1 measured on the Vibrating Sample Magnetometer (VSM; top panel) and Ta-Ie-1 measured on the Magnetic Property Measurement System (MPMS; bottom panel). (a) Moment versus field from room temperature (RT; purple) to 500°C (red) in steps of 25°C. (b) Three tested $B_{min}(T)$ curves: $B_{min} = B_{cl}$ (blue), $B_{min}(T) = B_{opt.\ 1}$ (orange) and $B_{min}(T) = B_{opt.\ 2}$ (green). (c) SRW diagrams for the three B_{min} options. $B_{min} = B_{cl}$ (blue) is distinct from the other two options (orange, green). (d) ATS-fit parameter $\mu_s(T)$. (e) Signal-to-noise in the ATS-window (squares) and the β-optimization window (diamonds). (f) Misfit relative to δ_{95} for both windows. (g) ATS-fit parameter $\beta(T)$. (h) ATS-fit parameter $\alpha(T)$. (i) ATS-fit parameter $\chi(T)$. Bottom panel: Diagrams for finding the optimal B_{min} amongst $B_{min} = 0.1, 0.2, 0.3, 0.4,$ and 0.5 T (color coded) for Ta-Ie-1 at 300 K. (j) Minimum misfit L_2-norms for β (vertical dashed lines). (k) Minimum misfit L_2-norms for μ_s in corresponding colors.
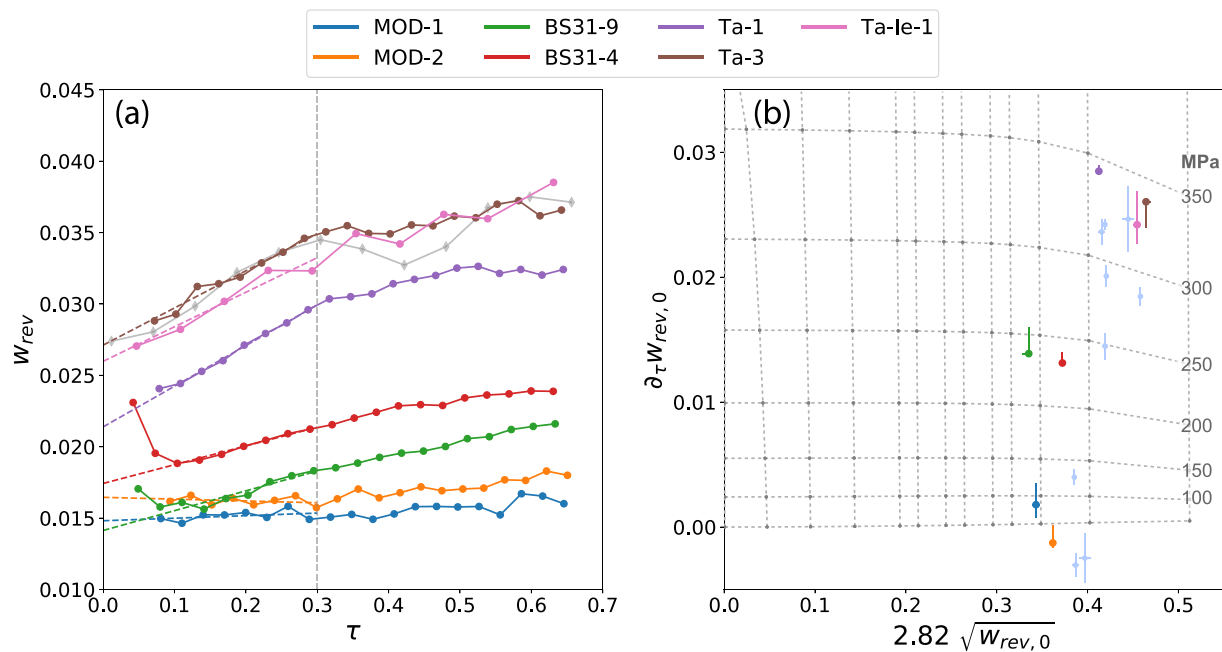
Figure 7. (a) Scaled reversible work (SRW) versus scaled temperature for seven natural specimens from Modum Serpentinite (MOD-1 and MOD-2), Bushveld (BS31-4 and BS31-9), and Taberg (Ta-1 and Ta-3 and Ta-Ie-1), with linear best-fit for $0.1 \leq \tau \leq 0.3$ (dashed lines). The gray diamonds follow the stress model (Béguin & Fabian, 2021) for $\Delta N = 0.45$ and $\sigma = 350$ MPa, with linear behavior for $\tau < 0.3$ (gray dashed vertical line), for larger τ values the model values are more curved reflecting the temperature dependence of $\lambda_{111}(T)$. (b) Interpretation of intercept $w_{rev,0}$ and slope $\partial_\tau w_{rev,0}$ in terms of effective demagnetizing factor ΔN and internal stress. The error bars reflect variability of best-fit line slopes in the range $0.1 \leq \tau \leq 0.3$ through at least eight data points after an interpolation of the data to steps of $\Delta \tau = 0.025$. Data for stressed and unstressed synthetic magnetite from Béguin and Fabian (2021) are plotted in light blue.

curves converge monotonically with increasing temperature. The largest difference as function of temperature is observed at low scaled fields, $b < 1.0$ (gray line in Figures 6b, 6e, and 6h).

The final result of all specimens, and the interpretation of the slope and SRW at $\tau = 0$, is visualized in Figure 7. All specimens show linear behavior for $\tau < 0.3$, the slopes and $w_{rev,0}$ values were calculated from the $\tau = 0.1 - 0.3$ interval. The approximately horizontal curves of $w_{rev}(\tau)$ for the two Modum specimens resulted in small slopes and plot in the corresponding low-stress regime below 100 MPa (Figure 7b). The $w_{rev,0}$ values correspond to approximate ΔN values of 0.35. The Bushveld specimens have smooth $w_{rev}(\tau)$ variations and show linear behavior over a large τ region, 0.1–0.4. Medium high slopes were estimated from the $\tau = 0.1 - 0.3$ interval, and $w_{rev,0}$ values result in ΔN values of 0.33–0.37. The Taberg specimens have highest $w_{rev}(\tau)$ curves. The curves show more variability and only show linear behavior for $\tau < 0.3$, for larger τ values the data follows the stress-model values of Béguin and Fabian (2021). High slopes and $w_{rev,0}$ values were obtained, translating to average stress and ΔN values between 320 and 340 MPa and 0.45–0.46, respectively. We observe an approximately constant offset between sister specimens from the same sample, e.g., Ta-1 and Ta-3 have an RT offset of approximately $\Delta w_{rev} = 0.0058$.

Rotation experiments were performed after the high-temperature SRW experiments. The results for the Taberg specimens are displayed in Figure 8, the results for the other specimens are available in Figure S12 of Supporting Information S1. The values of w_{rev} vary with the rotation angle between 0.035 and 0.043 for Ta-1 and between 0.043 and 0.049 for Ta-3. This variability corresponds to 14%–23% shape or textural anisotropy and could explain the observed offset in $w_{rev}(\tau)$ and $w_{rev,0}$. The results of the natural magnetite samples can be compared to the isotropic NTNU VSM calibration standard specimen, an yttrium-iron garnet (YIG) sphere with a diameter of about 2 mm and a magnetic saturation moment of 77.67 μA m². This YIG-specimen displayed a variation in μ_s between 75.8 and 80.5 μA m² ~6% (Figure S13 in Supporting Information S1). The signal change can partly be explained by the instrumental effects, where the 2θ signal is the movement of the sample in line with the pole pieces, left to right, and the 1θ signal results from movement back and forth perpendicular to the direction of the applied field (Kelso et al., 2002).
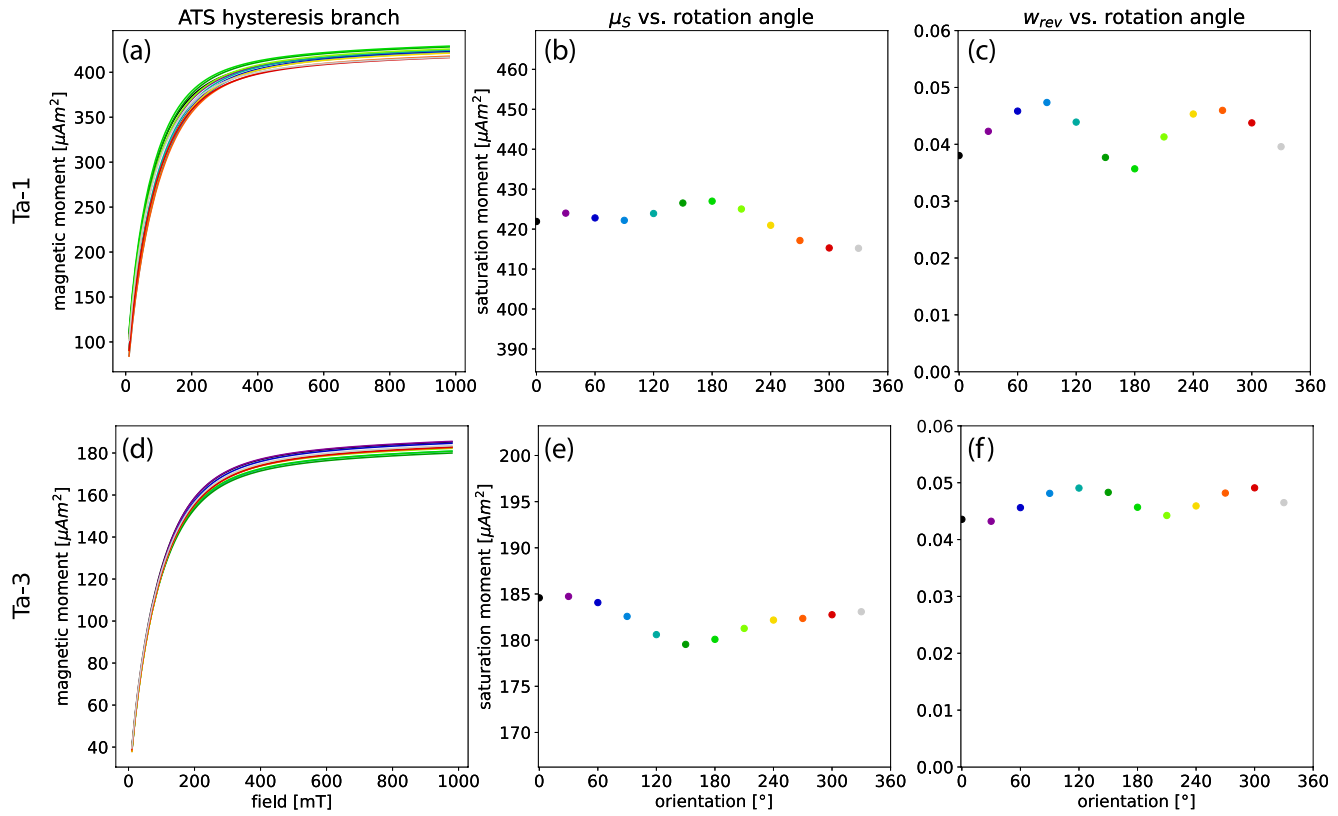
Figure 8. Postheating room temperature (RT) rotation experiment for `Ta-1` and `Ta-3`. Initial curves and hysteresis loops were measured with 30° rotation increments (a and d). A $B_{\min} = 0.25$ T was used for the ATS-fit. The range of the μ_s graph (b and e) is set to a 10% variation around the highest μ_s value. Both μ_s and w_{rev} change with rotation angle.

6. Discussion

6.1. Applicability of the SRW Method in Natural Samples

Our results present natural pilot samples containing magnetite as the dominant magnetic mineral and show that as in case of synthetic magnetite, a systematic analysis of the temperature-dependent SRW clearly separates magnetostatic and anisotropy-induced contributions. By assuming the literature magnetite values for saturation magnetization, cubic anisotropy, and magnetostrictive constants, the observed variation in SRW can be quantitatively expressed in terms of an effective magnetostatic factor ΔN and internal stress σ. Graphical representation of the scaled ATS curves in Figure 6 visually confirms that the systematic change of SRW corresponds to a monotonic convergence toward a purely geometrically—and thus magnetostatically—determined limit curve. Low-temperature deviations from this limit curve therefore clear evidence that additional magnetic torques need to be overcome to approach saturation. These general considerations do not depend on the specific value of spontaneous magnetization or other material constants, but assume a more or less homogeneous magnetic mineralogy. For the latter reason, we focus our study on magnetite-bearing samples.

6.2. New Methodical Approaches for Natural Samples

There are a number of technical aspects which complicate the SRW method for natural samples which are related to their lower homogeneity as compared to synthetic magnetite. The first parameter which requires separate determination is the temperature-dependent $M_s(T)$, which in turn requires an individual determination of T_C. Here, we estimate T_C from the extrapolation of the theoretical power law (Equation 2) to use it to scale the magnetization and external field. Due to the inhomogeneity of the natural samples, the T_C estimate based on the power law can differ from the T_C estimate based on the M_{si}-curves, because the two methods focus on different parts of the T_C distribution.

A separate effect may occur in the MPMS measurement for the Taberg specimen `Ta-Ie-1`, which took ~13 hr, while the VSM measurements on the other Taberg specimens only required ~4 hr. The increased time at elevated temperatures for `Ta-Ie-1` may lead to a rearrangement of residual noniron cations or vacancies within the magnetite lattice. Experiments of Price ([1981](#)) tried to homogenize the natural microstructures of Taberg specimens by heating them over a range of temperatures, from 490 to 730°C, with heating durations between 30 min and 100 days. The titanomagnetites initially contained oxidation-exsolution lamellae of ilmenite, lamellae of pleonaste, and a fine-scale cloth-texture intergrowth of ulvöspinel and magnetite (Price, [1981](#)). In specimens that were heated to ~680°C for a duration of 6 hr after annealing the cloth-texture had been homogenized, without effecting the pleonaste and ilmenite lamellae. From Figure 3 in Price ([1981](#)), we estimate the duration required to homogenize the microstructures in the Taberg specimens to be about 14 days, when heated to a typical temperature of 560°C as used in our experiments. Because our experiments had a total duration of ~4 hr in which the specimen is heated from RT to 550°C, we stay well below the duration where the microstructures homogenize to a measurable degree.

Another methodical optimization for natural samples concerns the fit of the ATS-law which depends on the window in which it is performed at different temperatures. We find that the consistency of the ATS-fits of μ_s and χ at different temperatures improves if (a) the values of $\beta(T)$ are consistently determined in a relatively small β-optimization window at high-field values, which still is large enough to minimize the effect of measurement noise, and (b) a larger ATS-fit window $[B_{\min}, B_{\max}]$ is used to fit the ATS-law for fixed β. The physical reason for using a small high-field window in the first step is to emphasize the fit quality in this window that determines β. Here, reversible magnetization processes that are different from the final alignment processes at high-field values are saturated. For example, in MD particles after denucleation of all domain walls, the magnetization structure may still contain swirl-like states that stretch out along the field direction. Each type of process will have its own ATS-law (Equation [1](#)) and their sum at intermediate field values will generate complex ATS behavior. By focusing on the high-field end, it is possible to saturate most of the intermediate field processes and thus provide the most reliable estimate for $\beta(T)$.

The above optimization procedures do not change the overall behavior of the values ultimately calculated for $w_{\mathrm{rev}}(T)$, but primarily reduce its temperature variation and lead to smoother and more reliable temperature variation. The best expression of this improvement is the systematic change of the ATS curve with temperature. And the scaled ATS curves converge with increasing temperature in a monotonically increasing way when the optimal scaling parameters are used (central column in Figure [6](#)).

6.3. Comparison of Sister Specimens

For each sample, two scaled measurements on sister specimens indicate that different specimens show very similar signal shapes, but that $w_{\mathrm{rev},0}$ can be offset by 10%–25% (in Figure [7a](#)). This offset is explained as a shape or textural anisotropy of the specimens. A good indication that this variation in w_{rev} is not purely due to instrumental influences, like a wobble of the sample rod, or imperfect centering between the two pole pieces is that the value of μ_s shows only a minimal variation with rotation angle that is below 3% (Figure [8](#)). The YIG-sphere rotation experimented further quantify possible offsets due to imperfect centering. The rotation experiment for the YIG-sphere with a diameter of about 2 mm showed, even after careful centering, a variation in μ_s of about 6%. We explain this relatively large variation by the small size of the YIG-sphere, whereby a small ±1 mm wobble completely displaces the sphere, while for a larger sample only a small fraction of the volume would be displaced by the same wobble.

6.4. Quantifying Stress and Anisotropy in the Natural Samples

The most important results of this study relate to the states of internal stress and demagnetization energy within natural magnetite. A most extreme case is the Modum sample which contains huge metamorphically grown magnetite crystals where little or no stress is expected, and our measurement results confirm this expectation. This sample also shows small values of ΔN indicating relatively low demagnetizing effects, even though the work against demagnetizing effects $w_{\mathrm{rev},0} \approx 0.016$ for `MOD-2` is still more than twice as large as the highest observed work against other anisotropies, which for `Ta-1` is $w_{\mathrm{rev}}(\tau = 0.3) - w_{\mathrm{rev},0} \approx 0.008$.

In Béguin and Fabian ([2021](#)), it was pointed out that even though the potential importance of internal stress in magnetite-ilmenite intergrowths has long been suggested (Moskowitz, [1993](#); Shive & Butler, [1969](#); Stacey

& Wise, 1967), and theoretical stress magnitudes at magnetite-ilmenite interfaces have been estimated by Price (1980), a quantitative experimental verification had not been performed. We here therefore focused on two sites where such interfaces are abundant. From Figure 7b, it can be inferred that for the Bushveld samples our measurements lead to average stress estimates of about 230 MPa, while the Taberg samples show average stresses up to 340 MPa for Ta-1. To our knowledge, this is the first direct measurement of these interface stresses. The results can be compared to the stress associated with the direct ulvöspinel-magnetite interface of Price (1980). Assuming an interface between TM60 and TM40, Price calculates stress magnitudes of 360 MPa for σ_x, perpendicular to the interface, and 660 MPa for $\sigma_y = \sigma_z$, within the interface. Such high stresses associated with coherent interfaces produced by exsolution are considerably larger than stresses normally withstood by the bulk material (Christian, 1975, Section 38; Price, 1980). The average stress depends on the fraction of the total magnetite volume close enough to the interface to experience the calculated stress. It therefore must be expected that the measured average stress is smaller than the calculated stress at the interface. For complex three-dimensional textures as they occur in BS31 and Ta, it is not exactly possible to predict the average value, although the SEM images indicate that the average distance to the nearest interface within the magnetite volume is <300 nm. The BS31 intergrowths show smaller average stress even though they have shorter wavelengths and correspondingly should have smaller average distance to the nearest interface. The higher average stress in Ta, might be related to the formation of the complex maze-like magnetite-ilmenite structure from an initial spinodal decomposition and later oxidation of ulvöspinel to ilmenite. The secondary oxidation could have further increased the internal stress in the surrounding magnetite intergrowths of Ta. Interestingly, besides the higher average stress, the $w_{rev}(\tau)$ curves of Ta closely follow the temperature dependence of λ_{111} and might therefore be more influenced by this magnetostriction constant than BS31 for which the curves decrease monotonically with temperature.

The B_u distributions measured in the FORC diagrams (Figure 2) indicated that magnetostatic interactions might have a stronger influence on the switching processes in the coarser Taberg than in the finer Bushveld intergrowth patterns. It appears consistent that also the results for ΔN in Figure 7 indicate a higher demagnetizing energy in the Taberg samples. There is a caveat in this conclusion because the FORC data are acquired in relatively small external fields, and changes in the internal magnetization structure dominate the B_u distribution. By contrast, ΔN is measured at high fields beyond B_{cl} and should mainly reflect the geometric texture of the magnetite. The agreement between these two interaction measures thus could indicate that magnetization stretching due to more complex helical or "postvortex" reversible magnetization patterns substantially contributes to ΔN as speculated in Béguin and Fabian (2021). The observations from Taberg and Bushveld specimens suggest that the larger exsolution patterns contain more complex magnetization structures which lead to wider B_u distributions and to a larger amount of magnetization stretching.

6.5. Outlook and Conclusions

The new SRW method provides several additional parameters that can be used to obtain a more detailed analysis of stress and demagnetization effects. The high-temperature limit of the scaled ATS magnetization curves provides direct information about the scaled fields b at which most of the alignment work $w_{rev,0}$ against the demagnetizing field is required. Because these b values depend on the specimen geometry they change with specimen rotation and effects of shape and texture will not be easy to separate.

The work difference $w_{rev}(T_0) - w_{rev,0}$ between the high-temperature limit ATS curve and, e.g., the RT T_0 ATS curve depends only on the internal magnetic energies of magnetocrystalline or stress origin. The dependence of this difference on b thus reflects the marginal distribution of stress values within the specimen. To fully exploit this stress distribution measurement requires better theoretical models of how the internal magnetization structures of magnetite respond to realistic internal stresses.

For the samples with microstructures resulting from spinodal-decomposition, we consistently find internal stress values >230 MPa, while for the metamorphic magnetite without lamellae resulted in almost stress-free magnetite crystals. These results confirm that the method of Béguin and Fabian (2021) can be successfully applied to natural rocks and quantitatively separates stress from magnetostatic effects. The shape of the $w_{rev(\tau)}$ curves possibly indicates the dominant interface stress and may hint to the type of oxidation processes. Our data displays a >20% variability in the demagnetizing energy parameter $w_{rev,0}$ between the sister specimens due to shape or textural anisotropy. The slope parameter $\partial_\tau w_{rev}$ indicates a variation of <5% due to stress anisotropy. This observation may lead to a new method of separately determining these anisotropies in magnetite-bearing rocks.

Data Availability Statement

All measured hysteresis data can be found in the Zenodo repository at https://doi.org/10.5281/zenodo.7615362 (Béguin et al., 2023a). The Python script used to evaluate the high-temperate hysteresis data for natural samples with the SRW method are available at https://doi.org/10.5281/zenodo.7950072 (Béguin et al., 2023b).

References

Akulov, N. S. (1930). Über ein Gesetz, das verschiedene Eigenschaften ferromagnetischer Kristalle miteinander verknüpft. *Zeitschrift für Physik*, *59*(3–4), 254–264. https://doi.org/10.1007/bf01341430

Akulov, N. S. (1931). Über den Verlauf der Magnetisierungskurve in starken Feldern. *Zeitschrift für Physik*, *69*(11–12), 822–831. https://doi.org/10.1007/bf01339465

Appel, E. (1987). Stress anisotropy in Ti-rich titanomagnetites. *Physics of the Earth and Planetary Interiors*, *46*(1–3), 233–240. https://doi.org/10.1016/0031-9201(87)90185-3

Appel, E., & Soffel, H. C. (1984). Model for the domain state of Ti-rich titanomagnetites. *Geophysical Research Letters*, *11*(3), 189–192. https://doi.org/10.1029/GL011i003p00189

Béguin, A., & Fabian, K. (2021). Demagnetization energy and internal stress in magnetite from temperature-dependent hysteresis measurements. *Geophysical Research Letters*, *48*, e2021GL096147. https://doi.org/10.1029/2021GL096147

Béguin, A., Fabian, K., Church, N. S., & McEnroe, S. A. (2023a). Data set for: Quantifying internal stress and demagnetization effects for natural multidomain magnetite and magnetite-ilmenite intergrowths [Dataset]. Zenodo. https://doi.org/10.5281/zenodo.7615362

Béguin, A., Fabian, K., Church, N. S., & McEnroe, S. A. (2023b). Python Script to analyze data for: Quantifying internal stress and demagnetization effects for natural multidomain magnetite and magnetite-ilmenite intergrowths [Dataset]. Zenodo. https://doi.org/10.5281/zenodo.7950072

Brown, W. F. (1940). Theory of the approach to magnetic saturation. *Physical Review*, *58*(8), 736–743. https://doi.org/10.1103/physrev.58.736

Brown, W. F. (1941). The effect of dislocations on magnetization near saturation. *Physical Review*, *60*(2), 139–147. https://doi.org/10.1103/physrev.60.139

Cawthorn, R. G., Lundgaard, K. L., Tegner, C., & Wilson, J. R. (2016). Lateral variations in plagioclase compositions, Main Zone, Bushveld complex, South Africa: Evidence for slow mixing of magmas in basinal structures. *Mineralogical Magazine*, *80*(2), 213–225. https://doi.org/10.1180/minmag.2015.079.7.12

Christian, J. (1975). *The theory of transformations in metals and alloys*. Pergamon. https://doi.org/10.1016/B978-008044019-4/50012-X

Church, N. S., Fabian, K., & McEnroe, S. A. (2016). Nonlinear Preisach maps: Detecting and characterizing separate remanent magnetic fractions in complex natural samples. *Journal of Geophysical Research: Solid Earth*, *121*, 8373–8395. https://doi.org/10.1002/2016JB013465

Dunlop, D. (2021). Magnetic hysteresis of magnetite at high temperature: Grain size variation. *Geophysical Journal International*, *226*(2), 816–827. https://doi.org/10.1093/gji/ggab138

Dunlop, D. J., & Özdemir, O. (1997). *Rock magnetism*. Cambridge University Press. https://doi.org/10.1017/CBO9780511612794

Egli, R. (2013). VARIFORC: An optimized protocol for calculating non-regular first-order reversal curve (FORC) diagrams. *Global and Planetary Change*, *110*, 302–320. https://doi.org/10.1016/j.gloplacha.2013.08.003

Fabian, K. (2003). Some additional parameters to estimate domain state from isothermal magnetization measurements. *Earth and Planetary Science Letters*, *213*(3–4), 337–345. https://doi.org/10.1016/S0012-821X(03)00329-7

Fabian, K. (2006). Approach to saturation analysis of hysteresis measurements in rock magnetism and evidence for stress dominated magnetic anisotropy in young mid-ocean ridge basalt. *Physics of the Earth and Planetary Interiors*, *154*(3–4), 299–307. https://doi.org/10.1016/j.pepi.2005.06.016

Fabian, K., Shcherbakov, V. P., & McEnroe, S. A. (2013). Measuring the Curie temperature. *Geochemistry, Geophysics, Geosystems*, *14*, 947–961. https://doi.org/10.1029/2012GC004440

Fabian, K., & von Dobeneck, T. (1997). Isothermal magnetization of samples with stable Preisach function: A survey of hysteresis, remanence, and rock magnetic parameters. *Journal of Geophysical Research*, *102*(B8), 17659–17677. https://doi.org/10.1029/97JB01051

Harrison, R. J., & Feinberg, J. M. (2008). FORCinel: An improved algorithm for calculating first-order reversal curve distributions using locally weighted regression smoothing. *Geochemistry, Geophysics, Geosystems*, *9*, Q05016. https://doi.org/10.1029/2008GC001987

Hjelmqvist, S. (1950). The titaniferous iron-ore deposit of Taberg in the south of Sweden. *Sveriges Geologiska Undersokning, Ser. C*, *512*, 1–55.

Hodych, J. P. (1973). Nonmagnetic uniaxial press with a tiltable piston. *Journal of Physics E: Scientific Instruments*, *6*(10), 1037–1039. https://doi.org/10.1088/0022-3735/6/10/026

Hodych, J. P. (1977). Single-domain theory for reversible effect of small uniaxial stress upon remanent magnetization of rock. *Canadian Journal of Earth Sciences*, *14*(9), 2047–2061. https://doi.org/10.1139/e77-175

Hodych, J. P. (1982). Magnetostrictive control of coercive force in multidomain magnetite. *Nature*, *298*, 542–544. https://doi.org/10.1038/298542a0

Hodych, J. P. (1986). Determination of self-demagnetizing factor-N for multidomain magnetite grains in rock. *Physics of the Earth and Planetary Interiors*, *41*(4), 283–291. https://doi.org/10.1016/0031-9201(86)90007-5

Hodych, J. P. (1990). Magnetic hysteresis as a function of low-temperature in rocks—Evidence for internal-stress control of remanence in multidomain and pseudo-single-domain magnetite. *Physics of the Earth and Planetary Interiors*, *64*(1), 21–36. https://doi.org/10.1016/0031-9201(90)90003-G

Hodych, J. P. (1996). Inferring domain state from magnetic hysteresis in high coercivity dolerites bearing magnetite with ilmenite lamellae. *Earth and Planetary Science Letters*, *142*(3–4), 523–533. https://doi.org/10.1016/0012-821x(96)00107-0

Hodych, J. P., & Matzka, J. (2004). Saturation magnetostriction and its low-temperature variation inferred for natural titanomaghemites: Implications for internal stress control of coercivity in oceanic basalts. *Geophysical Journal International*, *157*(3), 1017–1026. https://doi.org/10.1111/j.1365-246x.2004.02231.x

Hubert, A., & Schäfer, R. (1998). *Magnetic domains*. Springer.

Jackson, M., & Bowles, J. (2018). Malleable Curie temperatures of natural titanomagnetites: Occurrences, modes, and mechanisms. *Journal of Geophysical Research: Solid Earth*, *123*, 921–940. https://doi.org/10.1002/2017JB015193

Jackson, M., & Solheid, P. (2010). On the quantitative analysis and evaluation of magnetic hysteresis data. *Geochemistry, Geophysics, Geosystems*, *11*, Q04Z15. https://doi.org/10.1029/2009GC002932

Jøsang, O. (1966). *Geologiske og petrografiske undersøkelser i Modumfeltet*. Universitetsforlaget.

Kelso, P. R., Tikoff, B., Jackson, M. J., & Sun, W. (2002). A new method for the separation of paramagnetic and ferromagnetic susceptibility anisotropy using low field and high field methods. *Geophysical Journal International*, *151*(2), 345–359. https://doi.org/10.1046/j.1365-246X.2002.01732.x

Kersten, M. (1932). Zur magnetischen Analyse der inneren Spannungen. *Zeitschrift für Physik*, *76*(7–8), 505–512. https://doi.org/10.1007/bf01336732

Klapel, G. D., & Shive, P. N. (1974). High temperature magnetostriction of magnetite. *Journal of Geophysical Research*, *79*(17), 2629–2633. https://doi.org/10.1029/JB079i017p02629

Lindquist, A. K., Feinberg, J. M., Harrison, R. J., Loudon, J. C., & Newell, A. J. (2015). Domain wall pinning and dislocations: Investigating magnetite deformed under conditions analogous to nature using transmission electron microscopy. *Journal of Geophysical Research: Solid Earth*, *120*, 1415–1430. https://doi.org/10.1002/2014JB011335

McElhinny, M., & McFadden, P. (1999). *Paleomagnetism, continents and oceans* (Vol. 73). Academic Press.

McEnroe, S. A., Church, N., Fabian, K., Stange, M. F., & van Helvoort, A. T. J. (2022). An enigma in rock magnetism: Can microstructures in magnetite cause a threefold increase in the efficiency of NRM acquisition in the Stardalur basalts? *Geophysical Journal International*, *231*(2), 835–855. https://doi.org/10.1093/gji/ggac224

Moskowitz, B. M. (1993). Micromagnetic study of the influence of crystal defects on coercivity in magnetite. *Journal of Geophysical Research*, *98*(B10), 18011–18026. https://doi.org/10.1029/93JB01719

Munz, I. A., & Morvik, R. (1991). Metagabbros in the Modum complex, southern Norway: An important heat source for Sveconorwegian metamorphism. *Precambrian Research*, *52*(1), 97–113. https://doi.org/10.1016/0301-9268(91)90015-3

Néel, L. (1949). Théorie du traînage magnétique des ferromagnétiques en grains fins avec applications aux terres cuites. *Annales Geophysicae*, *5*, 99–136.

Pastore, Z., Church, N., & McEnroe, S. (2019). Multistep parametric inversion of scanning magnetic microscopy data for modeling magnetization of multidomain magnetite. *Geochemistry, Geophysics, Geosystems*, *20*, 5334–5351. https://doi.org/10.1029/2019GC008542

Pauthenet, R., & Bochirol, L. (1951). Aimantation spontanée des ferrites. *Journal de Physique et le Radium*, *12*(3), 249–251. https://doi.org/10.1051/jphysrad:01951001203024900

Petrovský, E., & Kapička, A. (2006). On determination of the Curie point from thermomagnetic curves. *Journal of Geophysical Research*, *111*, B12S27. https://doi.org/10.1029/2006JB004507

Price, G. (1979). Microstructures in titanomagnetites as guides to cooling rates of a Swedish intrusion. *Geological Magazine*, *116*(4), 313–318. https://doi.org/10.1017/S001675680004379X

Price, G. (1980). Exsolution microstructures in titanomagnetites and their magnetic significance. *Physics of the Earth and Planetary Interiors*, *23*(1), 2–12. https://doi.org/10.1016/0031-9201(80)90078-3

Price, G. (1981). Diffusion in the titanomagnetite solid solution series. *Mineralogical Magazine*, *44*(334), 195–200. https://doi.org/10.1180/minmag.1981.044.334.13

Robinson, P., McEnroe, S. A., Miyajima, N., Fabian, K., & Church, N. (2016). Remanent magnetization, magnetic coupling, and interface ionic configurations of intergrown rhombohedral and cubic Fe-Ti oxides: A short survey. *American Mineralogist*, *101*(3–4), 518–530. https://doi.org/10.2138/am-2016-5519

Sandecki, J. (2000). Mineralogical and genetical aspects of the Smålands Taberg Fe-Ti-V ore, Protogine Zone of southern Sweden. *GFF*, *122*(4), 351–358. https://doi.org/10.1080/11035890001224351

Shive, P., & Butler, R. (1969). Stresses and magnetostrictive effects of lamellae in the titanomagnetite and ilmenohematite series. *Journal of Geomagnetism and Geoelectricity*, *21*(4), 781–796. https://doi.org/10.5636/JGG.21.781

Stacey, F., & Wise, K. (1967). Crystal dislocations and coercivity in fine grained magnetite. *Australian Journal of Physics*, *20*(5), 507. https://doi.org/10.1071/ph670507

Stoner, E., & Wohlfarth, E. (1948). A mechanism of magnetic hysteresis in heterogeneous alloys. *Philosophical Transactions*, *240*, 599–642.

Tauxe, L. (2010). *Essentials of paleomagnetism*. University of California Press.

ter Maat, G. W., Fabian, K., Church, N. S., & McEnroe, S. A. (2020). Separating geometry-from stress-induced remanent magnetization in magnetite with ilmenite lamellae from the Stardalur basalts, Iceland. *Geochemistry, Geophysics, Geosystems*, *21*, e2019GC008761. https://doi.org/10.1029/2019GC008761

Yuan, K., Lee, S. S., Cha, W., Ulvestad, A., Kim, H., Abdilla, B., et al. (2019). Oxidation induced strain and defects in magnetite crystals. *Nature Communications*, *10*(1), 703. https://doi.org/10.1038/s41467-019-08470-0